Numerical study of liquid inclusion oscillations inside a closed 1-D microchannel filled with gas

M.-C. Duluc O.P. Le Maître V. Daru P. Le Quéré*

Preprint submitted to microfluidics and nanofluidics

Abstract

The motion of a liquid inclusion inside a 1D microchannel filled with gas and externally heated is simulated. An incompressible formulation is used for the liquid while a low Mach approximation is considered for the gas flow. Gas-liquid interfaces are captured using an ALE method. The whole liquid-gas system is shown to behave as a damped oscillator. Natural frequency of the linearized system and associated eigenmodes are first identified. Forced oscillations are investigated for different heating conditions (temperature or heat flux) at the microchannel ends. Detailed analyses are performed and reveal the main thermo-mechanical effects involved in the oscillations. The relevant parameters governing the dynamics are found out through a dimensionless analysis. Finally, heating conditions leading to non decaying oscillations of the liquid inclusion are proposed.

1 Introduction

Micro electromechanical elements (MEMS) make a wide use of fluid flows in microchannels ($<$ 1 mm). Due to the small size of the channels, these flows are associated with low values of the Reynolds number and are therefore laminar. Various operations like pumping, mixing, separation, ..., require a controlled motion of the fluid. This motion is often generated by the conversion of electrical energy into mechanical energy (displacement of a moving part), for instance in micropumps using piezoelectric membranes. Recent papers have shown that thermal actuation could be another suitable means to achieve fluid motion in microfluidic systems. This was achieved for instance using thermocapillary forces (displacement of a liquid plug, see [8]) or thermal expansion of a fluid (for micromixing [19] or deformation of a membrane in a micropump [4]). Beyond experimental evidences of thermal actuation feasibility for microfluidic systems, a better understanding of the physical phenomena involved, specifically those associated with microscales, is still needed to improve the design of such devices. To model these systems, one has to account for various physical effects, including thermodynamics, heat transfer and fluid dynamics.

The present study focuses on a simplified system consisting in a liquid inclusion inside a closed microchannel filled with a gas. The main objective is to investigate an idealized thermopneumatic actuator, which relies on heating/cooling at the channel ends to induce gas expansion/contraction in order to displace the liquid inclusion. Special attention is paid to oscillations of the liquid inclusion induced by periodic heating at the channel ends. As a first approach towards the modeling of such oscillatory flows, a simplified system is considered. In this approximation, variations of the

*LIMSI-CNRS, B.P. 133, 91403 Orsay Cedex, France - Tel.: +33-169858160 - Fax: +33-169858088 - emails [duluc,olm,daru,plq]@limsi.fr

flow in the channel transverse direction are disregarded, *i.e.* the flow is one-dimensional. Also, surface tension effects and wall friction, that are present in real systems, are ignored in the present model. It is clear that these effects may have a significant impact on the microflow dynamics. Nevertheless, this simplified model is expected to provide qualitative estimates of the essential scales and phenomena related to the thermopneumatic effects which are the focus of the present work. To be quantitatively relevant to actual microsystems, the model will need to be complemented to account for 2D effects (slip velocity, temperature jump, surface tension), this is the object of ongoing efforts.

The simulation of microfluidic flows rises various difficulties. A first aspect concerns the validity of a continuous description using the Navier-Stokes equations, as opposed to discrete models. A major difficulty in the simulation of microflows arises with the presence of different phases with high density ratio (such as for microbubbles in liquids) and contrasted compressibilities. This requires the use of robust numerical strategies capable of handling flows with discontinuities in the fluid properties in addition to the tracking of the interfaces between the phases. To address these difficulties, various numerical methods are proposed in the literature. For continuous models, as concerned in this paper, both Lagrangian (particle methods [11], Smoothed Particle Hydrodynamics [10],...) and Eulerian (finite -volumes, -differences, -elements,...see *e.g* the review papers [7, 5]) discretizations of the Navier-Stokes equations have been used previously. Similarly, numerical methods for the interfaces description can be gathered into Eulerian (level-set [16, 14], volume of fluid [18], Lattice-Boltzmann [22, 23],...) and Lagrangian (immersed interface method [20, 9], boundary element method [17]) approaches. All these techniques for the interface treatment rely on a single fluid domain involving a single set of equations for all phases and discontinuous properties across the interfaces (single field formulation).

In this work, we adopt an alternative strategy where different sets of governing equations are considered in the liquid and gas domains. An Arbitrary Lagrangian Eulerian (ALE) formulation is used to account for the deformations and displacements of the liquid and gas domains. Doing so, we are able to use governing equations well suited to the dynamics of each phase. Specifically the incompressible Navier-Stokes equations are used in the liquid domains, while compressibility is taken into account in the gas domains. Still, for microchannel flows, the gas velocity is small compared to the acoustic velocity and a low Mach number approximation is valid. The so-called low-Mach approximation as proposed in [12, 2] consists in filtering-out unwanted fast acoustic waves from the full set of compressible Navier-Stokes equations, while accounting for the state equation, and so, modeling of essential thermopneumatic effects. In [6], we have proposed a low-Mach model for the description of liquid-vapor flows. This model has been adapted to the present system by introducing the ALE method for the motion of interfaces. The resulting model allows for an accurate representation of the dynamics in each phase and of the interfaces location and conditions. These features are essential for the problem considered in this work, where thermopneumatic effects are the driving phenomenon.

The paper is organized as follows. The physical model of the system is presented in section 2. Details are provided on the interfaces boundary conditions and dynamics, while a numerical algorithm for the resolution of the resulting set of equations is given in Appendix A. In Section 3, a preliminary study, based on a simplified version of the model, is conducted to yield the natural frequencies of the oscillating liquid inclusion. The non linear dynamics of the liquid inclusion is subsequently investigated in Section 4 using different forcings applied at the channel ends. The relevant dimensionless parameters governing the dynamics are identified. Major findings are summarized in Section 5.

2 Physical model

2.1 Physical system

We consider the one-dimensional fluid system consisting of two layers of gas (Ω^1 and Ω^2) enclosing a liquid layer (Ω^l). The system is closed by two walls. The situation is depicted in Fig. 1. We denote l^1, l^2 and l^l the dimensions of the two gases and liquid domains respectively: $l^i = |\Omega^i|$. The total length of the system is $L = l^1 + l^2 + l^l$. We denote Γ^1 (resp. Γ^2) the gas-liquid interface between Ω^1 (resp. Ω^2) and Ω^l. Gaseous domains of small extension are considered in the present

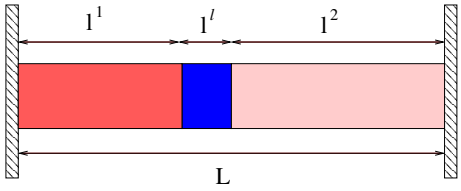

Figure 1: Schematic representation of the layered fluid system.

study ($l^i \lesssim 50\,\mu$m). The gas flow regime is first identified using the Knudsen number [3]:

$$\mathrm{Kn} = \lambda/l, \quad \lambda = \frac{1}{\sqrt{2}\pi d^2}\frac{kT}{P}. \tag{1}$$

The gas considered in the present study is air. The highest value likely to be encountered for the mean free path λ, corresponds to a temperature $T = 373.15$ K and to a pressure $P = 101325$ Pa. Using for the molecular diameter $d = 0.37$ nm, one obtains $\lambda \simeq 84$ nm. Characteristic length for the gas domains is $l \simeq 10^{-5}$ m, leading to characteristic Knudsen number of about 0.01. This value of the Knudsen number suggests that a continuous model is adapted to the simulation of the flow. Nevertheless, for $10^{-3} \leq \mathrm{Kn} \leq 10^{-1}$ slip conditions need to be considered at the domain boundaries [3]. For one-dimensional flows with fixed walls, the velocity slip condition is not relevant. This will be however necessary in the future extension of the model to domains with finite thickness. The temperature jump condition at the wall writes as:

$$T - T_w = \frac{F_t - 2}{F_t}\frac{2\gamma}{\gamma+1}\frac{\lambda}{Pr}\left(\frac{\partial T}{\partial x}\right)_{wall} \tag{2}$$

with the thermal accommodation coefficient F_t, the Prandtl number $\mathrm{Pr} = 0.7$, the specific heat ratio $\gamma = 1.4$ and $(\frac{\partial T}{\partial x})_{wall}$ the normal wall temperature gradient. Estimating the gradient as $\Delta T/l$, with $\Delta T \sim 80$ K the wall temperature rise in the simulations below, and assuming a perfectly diffuse reflection ($F_t = 1$), we obtain $T - T_w \sim 0.2$ K. This estimate, though not negligeable, is much less than ΔT. As a result, temperature jump will be neglected in the following. As for the slip velocity, temperature jump will have to be accounted for in two-dimensional systems.

2.2 Gas layers

The gases in layers 1 and 2 are the same, with thermal conductivity k^g, specific heat capacities c_p^g and c_v^g and viscosity μ^g. The gas is assumed ideal with state equation:

$$P^{1,2} = \rho^{1,2} r T^{1,2}, \tag{3}$$

where P^i is the thermodynamic pressure, ρ^i the gas density, T^i the gas temperature, and r the ideal gas constant. The characteristic Mach number, Ma, of the gas flows is $\mathrm{Ma} = U/C$ with $C = \sqrt{\gamma r T}$

the sound velocity, $\gamma = c_p^g/c_v^g$, and U the characteristic flow velocity based on the characteristic interface displacement velocity. Assuming $\mathrm{Ma} \ll 1$, the asymptotic analysis of the full system of compressible Navier-Stokes equations shows that, at leading order in Ma, the thermodynamic pressure in each gaseous domain is uniform:

$$P^i(x,t) = P^i(t), \quad i = 1,2.$$

This approximation corresponds to the low Mach model of the fully compressible Navier-Stokes equations, for which acoustic waves are filtered-out [12, 2]. The corresponding mass, momentum and energy conservation equations are [2, 12, 21]:

$$\frac{\partial}{\partial t}\rho^i + \frac{\partial}{\partial x}(\rho^i u^i) = 0, \tag{4}$$

$$\rho^i \frac{\partial}{\partial t}u^i + \rho^i u^i \frac{\partial}{\partial x}u^i = -\frac{\partial}{\partial x}\Pi^i + \mu^g \frac{\partial^2}{\partial x^2}u^i, \tag{5}$$

$$\rho^i c_p^g \left(\frac{\partial}{\partial t}T^i + u^i \frac{\partial}{\partial x}T^i\right) = k^g \frac{\partial^2}{\partial x^2}T^i + \frac{d}{dt}P^i, \tag{6}$$

where u^i is the gas velocity and Π^i the hydrodynamic pressure.

2.3 Liquid layer

The liquid has a thermal conductivity k^l and a specific heat capacity c^l. It is assumed incompressible, so for one-dimensional flow the velocity in Ω^l is uniform and the liquid density constant:

$$u^l(x,t) = u^l(t), \quad \rho^l(x,t) = \rho^l. \tag{7}$$

The momentum and energy conservation equations in the liquid consequently simplify to:

$$\rho^l \frac{d}{dt}u^l = -\frac{\partial}{\partial x}\Pi^l, \tag{8}$$

$$\rho^l c^l \left(\frac{\partial}{\partial t}T^l + u^l \frac{\partial}{\partial x}T^l\right) = k^l \frac{\partial^2}{\partial x^2}T^l. \tag{9}$$

It follows that the pressure gradient in the liquid is constant and proportional to the pressure difference at the interfaces:

$$\frac{\partial}{\partial x}\Pi^l = \frac{\Pi^l(\Gamma^2,t) - \Pi^l(\Gamma^1,t)}{l^l} \tag{10}$$

2.4 Boundary conditions and interface dynamics

At the interface Γ^i, the solutions in the gas and liquid domains satisfy the following continuity relations:

$$T^i(\Gamma^i,t) = T^l(\Gamma^i,t) \tag{11}$$

$$k^g \frac{\partial}{\partial x}T^i(\Gamma^i,t) = k^l \frac{\partial}{\partial x}T^l(\Gamma^i,t) \tag{12}$$

$$u^i(\Gamma^i,t) = u^l(\Gamma^i,t). \tag{13}$$

For the pressure on the interface, we identify the hydrodynamic pressure in the liquid domain with the thermodynamic pressure in the gas domain:

$$\Pi^l(\Gamma^i,t) = P^i(t) \quad i = 1,2. \tag{14}$$

Boundary conditions in the gaseous domains for $x = 0$ and $x = L$ are also needed. For the velocity, these are $u^i = 0$ as discussed previously. For temperature, Dirichlet and Neumann conditions will be used depending on the problem considered.

The liquid being incompressible, it is first remarked that both interfaces move with equal velocity so

$$\frac{d}{dt}\Gamma^1 = \frac{d}{dt}\Gamma^2, \quad \frac{d}{dt}l^1 = \frac{d}{dt}\Gamma^1 = -\frac{d}{dt}l^2, \tag{15}$$

and the dynamics of the liquid layer is entirely determined by $l^1(t)$: $u^l = dl^1/dt$. From the state equation Eq. (3), we have

$$\int_{\Omega^i} \frac{P^i(t)}{T^i(x,t)}dx = r\int_{\Omega^i} \rho^i(x,t)dx = rm^i, \tag{16}$$

where m^i is the mass of gas in Ω^i. Since we assume no phase change $dm^i/dt = 0$. Now, introducing the harmonic mean $\left\langle T^i(t)\right\rangle$ defined as:

$$\frac{1}{\langle T^i(t)\rangle} = \frac{1}{\langle T^i\rangle} \equiv \frac{1}{l^i}\int_{\Omega^i} \frac{dx}{T^i(x)}. \tag{17}$$

we obtain from Eq. (16)

$$P^i(t) = \frac{rm^i}{l^i(t)}\left\langle T^i(t)\right\rangle. \tag{18}$$

Then, using equations (14) and (10) the momentum equation (8) in the liquid becomes:

$$m^l\frac{d^2l^1(t)}{dt^2} = r\left[m^1\frac{\left\langle T^1\right\rangle}{l^1} - m^2\frac{\left\langle T^2\right\rangle}{l^2}\right]. \tag{19}$$

This differential equation yields time evolution of the liquid layer position. In Appendix A we provide a quick overview of the numerical methods and algorithms used for the resolution of the flow dynamics.

3 Linear dynamics of free systems

Before considering the full non-linear problem, we provide in this section a simplified linear analysis aiming at exhibiting the relevant time-scales of the problem. To this end, we focus on oscillations in the free system around an equilibrium state corresponding to a temperature T_e, pressure P_e, and domain sizes l_e^i. By free system, we mean the system without forcing, *i.e.* with both walls thermally insulated.

3.1 Linear eigen-problem

We start by deriving a first linear approximation for the dynamics of free oscillations of the layered system. We consider displacements of the interfaces, hereafter denoted $\epsilon(t)$, small compared to l_e^1 and l_e^2. We further assume in this first approach that: a) the displacement of the interfaces is slow compared to the sound velocity $C = \sqrt{\gamma r T_e}$; b) temperature in each gaseous domain is uniform and dependent on time only. The conservation equations for the gas internal energies ($e^i = m^i c_v^g T^i$) simplify consequently to

$$\begin{cases} m^1 c_v^g \dfrac{d}{dt}T^1 = -P^1\dfrac{d}{dt}\epsilon - q"_{1\to 2}, \\ m^2 c_v^g \dfrac{d}{dt}T^2 = P^2\dfrac{d}{dt}\epsilon - q"_{2\to 1}, \end{cases} \tag{20}$$

where $q''_{1\to 2} = -q''_{2\to 1}$ is the heat flux transferred from domain 1 to domain 2. The heat flux is classically modeled as

$$q"_{1\to 2} = \frac{T^1 - T^2}{R_l}, \tag{21}$$

where R_l is the thermal resistance of the liquid layer defined as $R_l \equiv l^l/k^l$. The equations of the simplified dynamics are then (20), (21) and the equation for the dynamics of the liquid layer:

$$m^l \frac{d^2}{dt^2}\epsilon = P^1 - P^2.$$

The mass conservation equations are in turn

$$m^1 = \rho_e l_e^1 = \rho^1(l_e^1 + \epsilon), \quad m^2 = \rho_e l_e^2 = \rho^2(l_e^2 - \epsilon), \tag{22}$$

with $\rho_e = P_e/rT_e$ the equilibrium density. With this latter relation, the perturbations equations become

$$\begin{aligned}
m^1 c_v^g \frac{d}{dt}T_1' &= -r\frac{m^1}{l_e^1+\epsilon}(T_e + T_1')\frac{d}{dt}\epsilon - \frac{T_1' - T_2'}{R_l},\\
m^2 c_v^g \frac{d}{dt}T_2' &= r\frac{m^2}{l_e^2-\epsilon}(T_e + T_2')\frac{d}{dt}\epsilon + \frac{T_1' - T_2'}{R_l},\\
\frac{d^2}{dt^2}\epsilon &= \frac{r}{m^l}\left[\frac{m^1}{l_e^1+\epsilon}(T_e + T_1') - \frac{m^2}{l_e^2-\epsilon}(T_e + T_2')\right],
\end{aligned}$$

where primes denote temperature perturbations from the equilibrium conditions: $T^i \equiv T_e + T_i'$. Finally, introducing the interfaces velocity $\dot\epsilon \equiv d\epsilon/dt$ and linearizing these equations, one obtains the following system of first order linear ODEs:

$$\begin{aligned}
m^1 c_v^g \frac{d}{dt}T_1' &= -P_e\dot\epsilon - \frac{T_1' - T_2'}{R_l},\\
m^2 c_v^g \frac{d}{dt}T_2' &= P_e\dot\epsilon + \frac{T_1' - T_2'}{R_l},\\
m^l \frac{d}{dt}\dot\epsilon &= -rT_e\left[\frac{m^1}{(l_e^1)^2} + \frac{m^2}{(l_e^2)^2}\right]\epsilon + r\left[\frac{m^1}{l_e^1}T_1' - \frac{m^2}{l_e^2}T_2'\right],\\
\frac{d}{dt}\epsilon &= \dot\epsilon.
\end{aligned}$$

This system of ODEs can be recast in the matrix form,

$$\frac{d}{dt}X = [A]X, \tag{23}$$

for the vector $X \equiv (T_1'\, T_2'\, \dot\epsilon\, \epsilon)^t$. The characteristics of small amplitude free oscillations are obtained by solving the eigen-problem

$$\lambda X = [A]X. \tag{24}$$

For simplicity, we focus on the case where $l_e^1 = l_e^2 = l_e$, so $m^1 = m^2 = m_e = \rho_e l_e$. In such conditions, $[A]$ has the following structure:

$$[A] = \begin{bmatrix} -\alpha & \alpha & -\beta & 0\\ \alpha & -\alpha & \beta & 0\\ \eta & -\eta & 0 & \kappa\\ 0 & 0 & 1 & 0 \end{bmatrix}. \tag{25}$$

Since the matrix $[A]$ is not symmetric, complex eigenmodes are expected. In fact, $[A]$ has two real eigenvalues, one of which being zero, and a complex conjugate pair of eigenvalues. Specifically, the first eigenvalue $\lambda = 0$ corresponds to a steady mode, with equal temperature perturbation in the two domains and unperturbed interfaces $\epsilon = \dot{\epsilon} = 0$ (see Fig. 2 for a schematic representation). The second real eigenvalue, $\lambda < 0$, corresponds to a monotonic decay of the perturbation with characteristic time-scale $\tau_d = -1/\lambda$. The eigenmode exhibits opposite temperature perturbation $T_1' = -T_2'$ and consistent interface perturbations (*e.g.* $\dot{\epsilon} = \lambda\epsilon$). Finally, the two conjugate modes correspond to damped oscillations with frequency $f_o = |Im(\lambda)|/2\pi$ and damping time scale $\tau_o = -1/Re(\lambda)$.

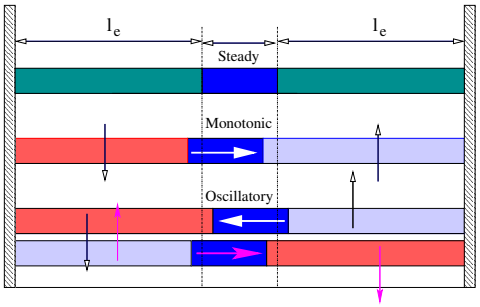

Figure 2: Schematical representation of the eigenmodes for the linearized system dynamics (vertical arrows represent evolutions of gas temperatures and horizontal arrows the interfaces velocity).

The characteristic damping times τ_d and τ_o of the monotonic and oscillatory dynamics are reported as a function of R_l in Fig 3 for an air-water system with $L = 100$ μm $l_e = 45$ μm, $\rho^l = 1000$ kg/m^3, $P_e = 101325$ Pa, $T_e = 293.15$ K, $r = 286.69$ J kg^{-1}K^{-1} and $c_v^g = 714$ J kg^{-1}K^{-1}. It shows that the monotonic decay is faster as the thermal resistance of the liquid $R_l \to 0$. This expected behavior has to be contrasted with the oscillatory damping time scale τ_o. Indeed, if τ_o increases with liquid thermal resistance when R_l becomes higher than $> 10^{-4}$ Km^2W^{-1}, it also increases when $R_l \to 0$. This trend suggests that two mechanisms are competing in the oscillatory dynamics, a different one being dominant depending on the liquid thermal resistance. This competition between oscillatory mechanisms is even more stressed in Fig. 4 where plotted is the oscillation frequency f_o as a function of the thermal resistance R_l: the f_o value levels down and up as R_l goes to 0 or ∞, with a transition region corresponding to $R_l \in [10^{-5}, 10^{-3}]$. These two mechanisms call for further explanations.

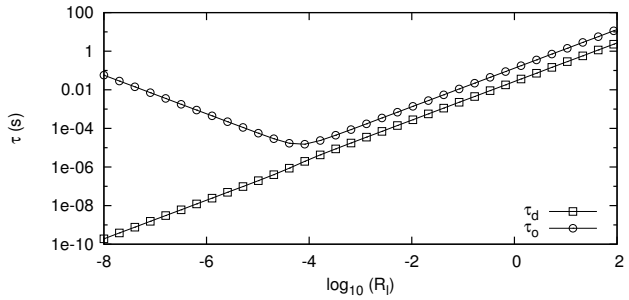

Figure 3: Dependence of the damping time-scales with the liquid thermal resistance R_l.

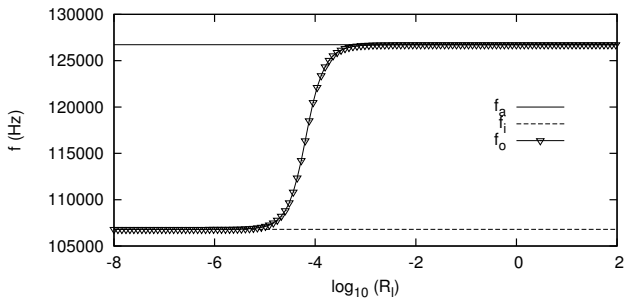

Figure 4: Dependence of the oscillatory frequency with the liquid thermal resistance R_l.

3.2 Limiting cases

The first limiting case corresponds to $R_l \to \infty$. In this case, for small perturbations the heat fluxes $q''_{1\to 2}$ and $q''_{2\to 1}$ becomes negligible so the transformations in the two gas domains can be idealized as adiabatic transformations. As this simplified model does not account for mechanical or thermal irreversibility, one may use the classical isentropic relations for an ideal gas:

$$P^i {l^i}^\gamma = P_e {l_e^i}^\gamma, \tag{26}$$

The adiabatic dynamics of the liquid layer turns to

$$m^l \frac{d}{dt}\dot{\epsilon} = P^1 - P^2 = P_e \left[\frac{{l_e^1}^\gamma}{(l_e^1 + \epsilon)^\gamma} - \frac{{l_e^2}^\gamma}{(l_e^2 - \epsilon)^\gamma} \right]. \tag{27}$$

Linearization of this equation about $\epsilon = 0$ gives:

$$m^l \frac{d^2}{dt^2}\epsilon \approx -P_e \gamma \frac{l_e^1 + l_e^2}{l_e^1 l_e^2}\epsilon. \tag{28}$$

This is the classical equation of an undamped linear oscillator, with natural frequency f_a as

$$2\pi f_a = \sqrt{\frac{P_e \gamma}{m^l} \frac{l_e^1 + l_e^2}{l_e^1 l_e^2}}. \tag{29}$$

This frequency is reported in Fig. 4 which shows that indeed $f_o = f_a$ for sufficiently large values of the liquid thermal resistance.

On the other hand, for a low thermal resistance, the heat fluxes q'' are very efficient at restoring equal temperatures in the two gas domains so the approximation $T'_1 \approx T'_2$ is valid and the second term in the r.h.s. of the ODE for $\frac{d}{dt}\dot{\epsilon}$ is negligible compared to the first one. Consequently, this equation can be recast in

$$m^l \frac{d}{dt}\dot{\epsilon} \approx -P_e \frac{l_e^1 + l_e^2}{l_e^1 l_e^2}\epsilon, \tag{30}$$

which again corresponds to an undamped linear oscillator with natural frequency f_i as

$$f_i = \frac{1}{2\pi}\sqrt{\frac{P_e}{m^l} \frac{l_e^1 + l_e^2}{l_e^1 l_e^2}} = \frac{1}{\sqrt{\gamma}} f_a. \tag{31}$$

This frequency is also reported in Fig. 4, where f_o is indeed seen equal to f_i for low values of the liquid thermal resistance.

3.3 Discussion

From the developments above, the following conclusions can be drawn. For systems with a liquid layer offering a large thermal resistance, weakly damped oscillations with characteristic frequency given by Eq. (29) are to be expected. Temperature deviations T_1' and T_2' are then mostly governed by adiabatic processes as the gas domains are alternatively compressed and expanded. Since compression and expansion occur with opposite phase in the two domains, the difference in temperature fluctuations yields a heat flux q'' between the two domains that induces a weak damping through irreversible heat conduction phenomenon. On the contrary, when the liquid thermal resistance is sufficiently low, the compression and expansion processes are essentially isothermal, with frequency given by Eq. (31), as any temperature rise in a compressed domain is quickly resorbed by mean of conductive heat transfer toward the second domain. This prevent the emergence of significant temperature differences. This process is therefore associated to low thermal irreversibility. As a result is observed a weak damping of the oscillations. Systems in the intermediate range of thermal resistance ($R_l \in [10^{-5}, 10^{-3}]$) combine the two mechanisms and so experience larger damping rates with intermediate oscillatory frequency $f_o \in [f_i, f_a]$.

The analysis in this section has dealt with a rough idealization of the liquid layer modeled as a medium characterized by its mass m^l and thermal resistance R_l only. The actual systems, as simulated in the following, are however more complex as the liquid can store energy ($q''_{1\to 2} = -q''_{2\to 1}$ does not necessarily hold) and will be the source of additional thermal irreversibility by inducing non-uniform temperature fields, especially for a liquid layer with large thermal inertia. Still, the time scales found through the linear analysis are expected to be relevant for the detailed system.

4 Dynamics of forced systems

In the following, we consider systems which are initially at an equilibrium state (T_e, P_e, l_e^l) and subsequently disturbed. Different types of forcing are considered: imposed temperature or imposed heat flux at one or two of the channel ends. We focus on water/air system with, otherwise explicitly stated, the following nominal physical properties (in SI units -kg, J, m, W, K-): $\rho^l = 1000$, $c^l = 4184$ and $k^l = 0.6$ (liquid water), and $c_p^g = 1000$, $r = 286.69$, $k^g = 0.0256$ and $\mu^g = 1.82\,10^{-5}$ (air). The peak gas velocity is 0.4 m/s which corresponds to a Reynolds number equal to 1.2. The flow is therefore laminar. Variations of physical properties are disregarded. In addition, the geometry of the system at equilibrium is $L = 10^{-4}\ m$, $l_e^1 = 45\,10^{-6}\ m$ and $l^l = 10^{-5}\ m$, with thermodynamical conditions $P_e = 101325\ Pa$, $T_e = 293.15\ K$. This situation will be referred in the following as the *nominal case*

4.1 Temperature forcing

For this forcing, a sudden change in temperature is imposed on the left wall ($x = 0$):

$$T(x = 0, t > 0) = T_w \neq T_e,$$

while the right wall ($x = L$) is assumed perfectly insulated. For these boundary conditions there exists an asymptotic steady state for $t \to \infty$ given by:

$$T(x, \infty) = T_w, \quad P(x, \infty) = P_w \equiv \frac{P_e T_w}{T_e}, \quad \forall x \in [0, L].$$

Moreover, the asymptotic geometry corresponds to the equilibrium one:

$$\lim_{t\to\infty} l^i(t) = l_e^i. \tag{32}$$

We set $T_w = 373.15\,\mathrm{K} > T_e$, and the full low-Mach number simulation is performed with numerical parameters: $\Delta t = 5\,10^{-8}$s and spectral elements with polynomial order 25 and 10 in the gas and liquid domains respectively. These numerical parameters were carefully selected from a convergence analysis (not shown).

Fig. 5 presents the evolution with time of the left gas domain extension $l^1(t)$. It is seen that the dynamics can be split into two distinct stages: the liquid layer first undergoes a rapid oscillatory motion with a net displacement toward the right of the domain, and subsequently slowly moves back monotonically to the asymptotic position. The first stage ($t < 150\ \mu$s) is associated with significant velocities ($\sim 1\ ms^{-1}$), though much less than the speed of sound. The evolutions of the thermodynamical pressures within the two gaseous media, reported in Fig. 6, are seen to be responsible for the oscillatory motion of the liquid layer. In fact, the oscillatory motion during the first stage presents similar characteristics with the ones developed in the linear analysis of the previous section, both in terms of frequency and damping time scale. During the second stage ($t > 150\ \mu$s), Fig. 6 shows that both pressures are essentially equal leading to much lower acceleration levels and a slow motion of the liquid layer toward the asymptotic state as a result. We now analyze in detail these two stages, starting with the second one for the sake of comprehension.

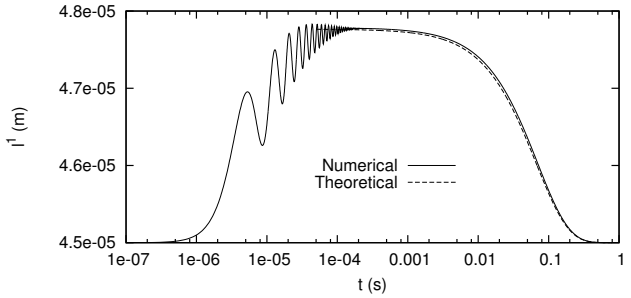

Figure 5: Location of the first interface as a function of time: comparison of numerical result and theoretical value from Eq. (42).

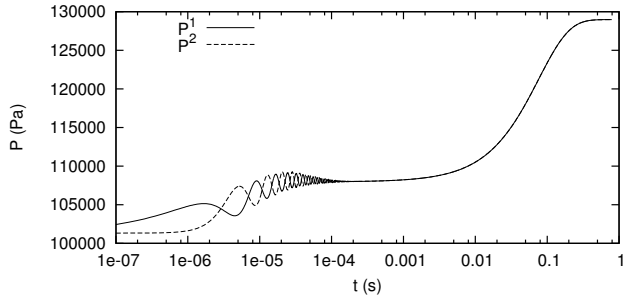

Figure 6: Pressures in the gas domain as a function of time. Nominal case.

4.1.1 Second stage

The second stage is characterized by essentially equal pressures in the gaseous domains. This allows for further simplifications of Eq. (19) to obtain:

$$l^1(t) \approx \left(L - l^l\right)\left(1 + \frac{l_e^2}{l_e^1}\frac{\langle T^2(t)\rangle}{\langle T^1(t)\rangle}\right)^{-1} \tag{33}$$

Eq. (33) shows that the displacement of the liquid layer depends on the geometric parameters (L, l^l and l_e^1) and on the harmonic means for the gas temperatures within each gaseous medium: the motion during the second stage is a quasi-static process, entirely governed by the thermal fields. Time evolution of the temperature fields, derived from numerical simulations, is presented in Fig. 7. During the second stage, temperature of the liquid layer is roughly uniform due to its significantly larger thermal conductivity than the gas one. The temperature distribution in the second gas ($x \in \Omega^2$) is also roughly uniform and equal to the liquid temperature. This logically stems from the adiabatic wall at $x = L$. In the first gas domain is observed a quasi linear temperature profile. This suggests to approximate the temperature distributions in the gaseous domains during the second stage as:

$$\begin{cases} T^1(x,t) \approx T_w + x(T^l(t) - T_w)/l^1, & x \in \Omega^1, \\ T^2(x,t) \approx T^l(t), & x \in \Omega^2. \end{cases} \tag{34}$$

Using these approximated temperature profiles, one can estimate the harmonic means $\langle T^1(t) \rangle$ and

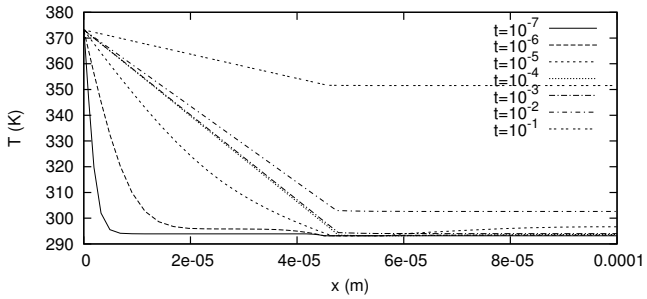

Figure 7: Temperature fields at different times t as indicated. Nominal case.

$\langle T^2(t) \rangle$ to be:

$$\begin{cases} \langle T^1(t) \rangle = \dfrac{(T^l(t) - T_w)}{\ln(T^l(t)/T_w)}, \\ \langle T^2(t) \rangle = T^l(t). \end{cases} \tag{35}$$

We now need to derive an expression for temperature evolution in the liquid layer. Liquid is assumed to be incompressible, thus energy exchanged with its surroundings is solely thermal energy. Thus, one has for energy conservation:

$$\rho^l \frac{d}{dt} \int_{\Omega^l} e^l dx = q"(\Gamma^1, t) - q"(\Gamma^2, t) \tag{36}$$

where $e^l = c^l T^l$ is the specific internal energy of the liquid phase. Now considering temperature profiles in the gaseous media given by Eq. (34), one obtains at the liquid boundaries:

$$\begin{cases} q"(\Gamma^1, t) \simeq k^g \dfrac{T_w - T^l}{l_e^1}, \\ q"(\Gamma^2, t) \simeq 0. \end{cases} \tag{37}$$

Reminding that thermal conductivity of the liquid is much higher than the gaseous one, continuity of the heat flux at the gas-liquid interface Γ^1 yields:

$$\left(\frac{\partial T^l}{\partial x} \right)_{\Gamma^{1+}} \ll \left(\frac{\partial T^1}{\partial x} \right)_{\Gamma^{1-}}. \tag{38}$$

Temperature is thus assumed to be uniform in the liquid domain, and the energy conservation now reads:

$$m^l c^l \frac{d}{dt} T^l = k^g \frac{T_w - T^l}{l_e^1}. \tag{39}$$

Time evolution of the liquid temperature is then given by a first order ordinary differential equation:

$$\rho^l l^l c^l \frac{dT^l}{dt} = k^g \frac{T_w - T^l}{l_e^1}, \tag{40}$$

which after integration yields

$$T^l(t) = T_w + (T_e - T_w) e^{-t/\tau}, \quad \tau \equiv \rho^l l^l c^l / k^g. \tag{41}$$

Time evolution of the liquid temperature is plotted in Fig. 8. Time evolution of the temperature on the interfaces ($x = \Gamma^1$ and $x = \Gamma^2$) and on the adiabatic wall ($x = L$) derived from the numerical simulation are also presented. An excellent agreement, for the second stage, is reported between the theoretical estimate in Eq. (41) for the liquid temperature and the computed evolutions of the temperature at the interfaces. Now, introducing in Eq. (33) the expressions of the harmonic means

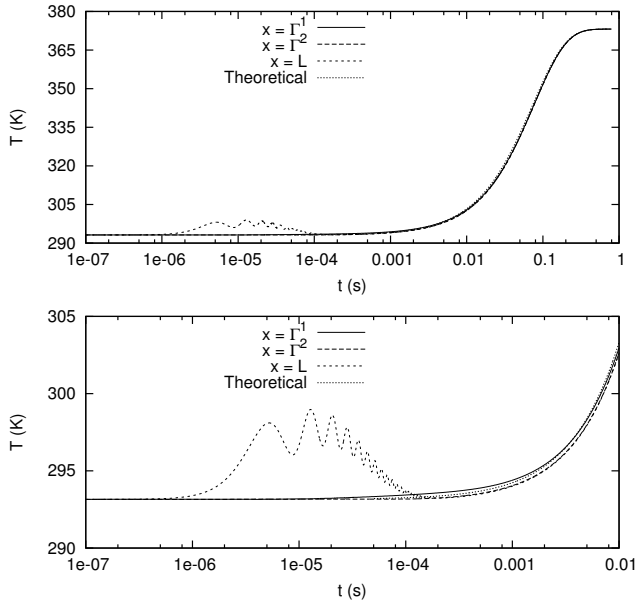

Figure 8: Temperature of the interfaces and at the insulated wall as a function of time for $t \in [10^{-7}, 1]$ (top plot) and details for $t \in [10^{-7}, 10^{-2}]$ (bottom plot). Also provided is the theoretical estimate given by Eq. (41).

$\left\langle T^1(t) \right\rangle$ and $\left\langle T^2(t) \right\rangle$ given by Eq. (35) and using Eq. (41), one obtains an analytical expression for the location of the first interface:

$$l^1(t) = \frac{\left(L - l^l\right)}{1 + \dfrac{l_e^2}{l_e^1} \dfrac{T_w + (T_e - T_w) e^{-t/\tau}}{(T_e - T_w)\, e^{-t/\tau}} \ln\left(1 + \dfrac{T_e - T_w}{T_w}\, e^{-t/\tau}\right)}. \tag{42}$$

This result, whose validity is limited to the second stage, is compared in Fig. 5 with the result of the numerical simulation. An excellent agreement is reported for the second phase. The theoretical

model developed here relies on the essential assumption that temperature is uniform within the liquid layer. Close inspection of the temperature plots in Fig. 8 reveals that the temperatures of the interfaces in the simulation are not exactly equal, though the theoretical estimate in Eq. (41) provides an excellent approximation of the interfaces temperature. These differences are deemed due to the finite conductivity of the liquid. To support this claim, a new simulation was performed with a liquid thermal conductivity 100 times larger than its nominal value. Using $k^l = 60$ is indeed seen to improve the agreement between the simulation and the theoretical model, as one may appreciate from Fig. 9 where plotted are the first interface location as computed for $k^l = 0.6$, $k^l = 60$ and predicted by Eq. (42).

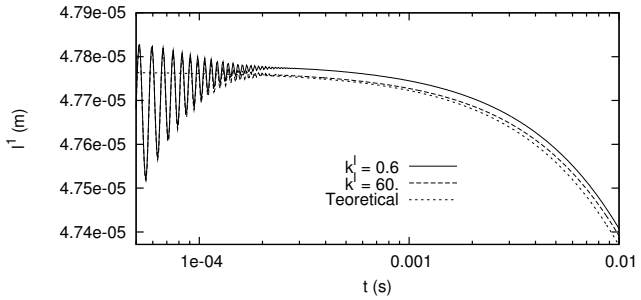

Figure 9: Comparison of the first interface location computed for $k^l = 0.6$ and $k^l = 60$ with the theoretical model in Eq. (42).

The theoretical model also allows for quantitative assessment of the maximum displacement, denoted l_m, of the liquid layer from its equilibrium position:

$$l_m \equiv \max_t \left(l^1(t) - l_e^1\right) = \frac{L - l^l}{1 + \dfrac{l_e^2}{l_e^1}\dfrac{\ln(T_w/T_e)}{T_w/T_e - 1}} - l_e^1. \tag{43}$$

The theoretical maximum displacement is seen to depend on the geometric parameters (L, l^l, l_e^1) and the temperature ratio T_w/T_e, but not on the fluid properties. In particular, l_m is a static quantity that does not depend on the liquid density. Fig. 10 depicts l_m for the nominal geometrical parameters L and l^l, but for different ratio of the gaseous domains extensions and for different temperature ratio T_w/T_e. As one may have anticipated, the magnitude of l_m increases as T_w/T_e deviates from 1, and is maximal when the gaseous domains have comparable sizes. High temperature ratio is nevertheless required to obtain a substantial displacement of the liquid layer.

4.1.2 First stage

The dynamics during the first stage ($t < 150\,\mu$s) is essentially governed by the pressure difference between both gaseous media (see Fig. 6). The analysis of free oscillations presented in section 3 highlighted specific frequencies related to the natural oscillation processes. The frequency, which depends on the liquid thermal resistance, ranges between f_i given by Eq. (31) and f_a given by Eq. (29). The numerical values associated to the present test-case are $R_l = 1.7\ 10^{-5} Km^2W^{-1}$, $f_i \sim 107$ kHz and $f_a \sim 126$ kHz. One observes from Fig. 4 that the present R_l value leads to a frequency very close to f_i. One therefore expects natural oscillations to have a period close to $t_i = 1/f_i \simeq 9.4\ \mu$s. Indeed, one observes in Fig. 5 that this value closely matches with the interface oscillations reported during the first stage.

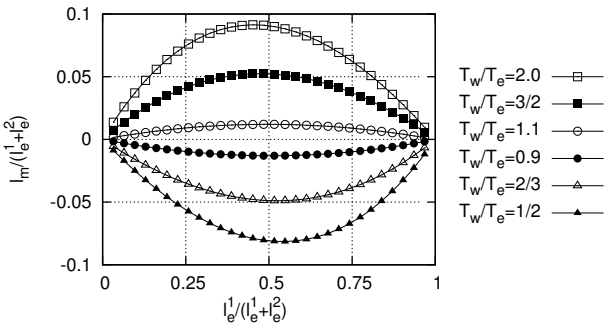

Figure 10: Normalized maximum displacement of the liquid layer as function of the extensions of the two gaseous domains and for different temperature ratios as indicated. $L = 10^{-4}$m, $l^l = 10^{-5}$m.

The temperature fields presented in Fig. 7, show that the temperature increases rapidly in the heated gas during early times. A linear temperature profile is achieved in a time period of about 100 μs, which nearly corresponds to the duration of the first phase. This temperature field appears very similar that one would observe in a purely diffusive regime. Now using the characteristic time for heat diffusion,

$$t_d = \frac{(l_e^1)^2}{\alpha^g} = (l_e^1)^2 \frac{\rho_e^1 c_p^g}{k^g}, \tag{44}$$

one obtains for the present situation $t_d \simeq 95$ μs, which indeed is a close estimate of the time period required to achieve a linear temperature profile in the heated gas. Due to the high thermal inertia of the liquid layer, the liquid temperature is not much affected during the first stage and remains close to its initial value T_e (see Fig. 7 and Fig. 8).

Evolutions of temperature in the second gaseous layer ($x \in \Omega^2$) deserve a few comments. We recall that the second gas layer is thermally insulated on the right wall ($x = L$). The temperature of the liquid layer remaining essentially constant during the first stage (see Fig. 7), one would thus expect the temperature in Ω^2 to do so. However, significant variations of the temperature in Ω^2 are reported for early times. This can be seen from the evolution of the insulated wall temperature ($x = L$) in the bottom plot of Fig. 8. These variations are due to compressibility effects: the internal energy of the gas and therefore its bulk temperature increases (decreases) by the work of compression (expansion) induced by the velocity of the liquid layer. The bulk temperature rise in Ω^2 disappears as the velocity of the liquid layer becomes small *i.e.* at the end of the first stage $t \sim 10^{-4}$ s.

4.2 Flux forcing

Forcing with imposed constant heat flux is now considered. We denote q'' the forcing heat flux applied at one of the wall, while the second one remains thermally insulated. The magnitude of the heat flux is set to $|q''| = 4.5\,10^4\,\mathrm{Wm}^{-2}$, a value corresponding to $k^g(T_w - T_e)/l_e^1$ with $T_w = 373.15\,\mathrm{K}$ and $T_e = 293.15$ K as previously. Fluids properties and equilibrium state are kept unchanged. Contrary to the former situation (temperature forcing), there is no asymptotic steady state for the flux forcing. Two cases are simulated using the low-Mach number model, one with a positive heat flux and one with a negative heat flux. When positive, the heat flux is imposed at the left wall ($x = 0$), while for negative heat flux it is imposed on the right wall ($x = L$). This ensures a displacement of the liquid layer in the the same direction for the two cases to ease comparison.

The computed locations of the first interface ($x = \Gamma^1$) are reported in Fig. 11 for $q'' > 0$ and $q'' < 0$. Once again, observed are fast displacements of the liquid layer (first stage) followed by

slower motions (second stage). Also similar to the temperature forcing is the duration of the first

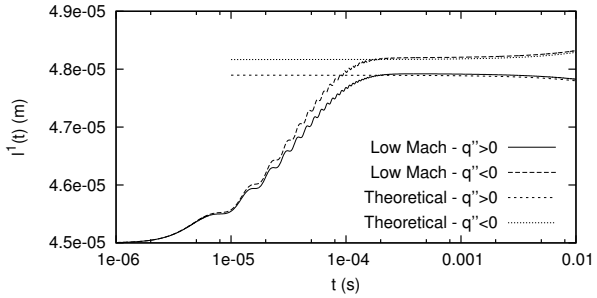

Figure 11: Evolution in time of the first interface location for positive heat flux ($q'' > 0$) at the left wall and negative heat flux ($q'' < 0$) at the right wall. Also plotted are the theoretical locations. Nominal case.

stage which extends up to $t \simeq 150\ \mu$s, as it is still associated to the characteristic time for heat diffusion. However large amplitude oscillations observed for the temperature forcing have lower amplitude here. The liquid layer undergoes a quick displacement to the right before reaching a plateau at the end of the first stage. Interesting enough, the motion during the first stage and achieved displacement at its end both depend on the sign of the imposed heat flux: this asymmetry which is due to the gas compressibility develops as time elapses.

Another analytical approximation is derived for this second stage based on the following assumptions:

1. temperature in the liquid is uniform ($k^l \gg k^g$);
2. acceleration of the liquid layer can be neglected;
3. temperature profile in the gas domain in contact with the heated wall is linear.

To avoid lengthy developments, we restrict ourself to the case $q'' > 0$, the case of $q'' < 0$ being similar. The linear temperature profile in Ω^1 is:

$$T(x,t) = -\frac{q''}{k^g}\left(x - l^1(t)\right) + T^l(t), \quad x \in \Omega^1. \tag{45}$$

As the acceleration of the liquid layer is neglected, Eq. (33) giving the position of the first interface still holds with the harmonic means now having for expressions:

$$\begin{aligned} \left\langle T^2(t)\right\rangle &= T^l(t), \\ \left\langle T^1(t)\right\rangle &= \frac{q''}{k^g} l^1(t) \left(\ln \frac{T^l(t)}{T^l(t) + \frac{q''}{k^g} l^1(t)} \right)^{-1}. \end{aligned} \tag{46}$$

Energy conservation for the liquid layer reads:

$$\rho^l c^l l^l \frac{dT^l}{dt} = q''. \tag{47}$$

After integration, it gives the liquid temperature law:

$$T^l(t) = \frac{q''}{\rho^l c^l l^l} t + T_e. \tag{48}$$

Inserting Eqs. (46) and (48) into Eq. (33), one obtains the following transcendental equation for the first interface location:

$$l^1(t) + l^l - L = -\frac{{l^2}_0}{{l^1}_0}\frac{q''}{k^g}\left(\frac{q''}{\rho^l c^l l^l}t + T_e\right)\ln\left(\frac{\frac{q''t}{\rho^l c^l l^l} + T_e}{\frac{q''}{k^g}l^1(t) + \frac{q''}{\rho^l c^l l^l}t + T_e}\right). \tag{49}$$

This theoretical estimate is plotted in Fig. 11 for the two values of the heat flux. An excellent agreement between the theoretical model and the numerical simulations is observed. Time evolutions of temperature at the insulated wall ($x = L$ for $q'' > 0$ and $x = 0$ for $q'' < 0$) and at the interfaces ($x = \Gamma^1(t)$ and $x = \Gamma^2(t)$) are presented in Fig. 12 for the two heating conditions. The liquid temperature given by Eq. (48) is also plotted on the graph. A good agreement is observed between computed interface temperatures ($x = \Gamma^1$ and $x = \Gamma^2$) and the analytical liquid temperature given by Eq. (48).

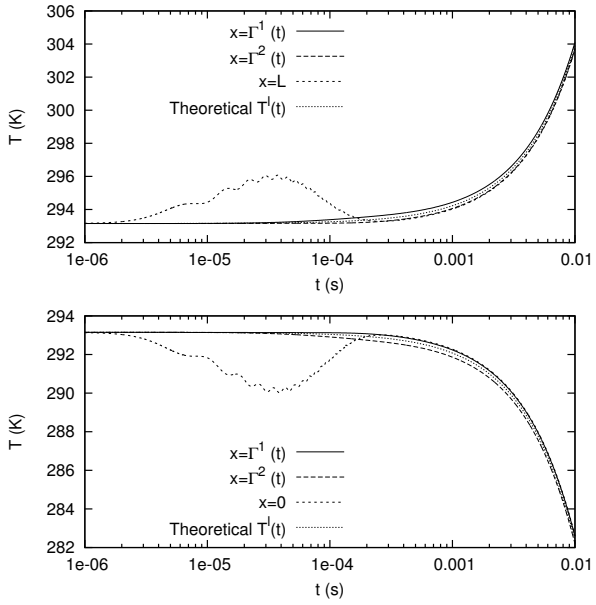

Figure 12: Top plot: evolution in time of the wall and interface temperatures for positive heat flux ($q'' > 0$) at the left wall (right wall is insulated). Bottom plot: evolution in time of the wall and interface temperatures for negative heat flux ($q'' < 0$) at the right wall (left wall is insulated). Nominal case.

The model is therefore suitable to explain the system behavior during the second phase (at least up to the point where temperatures are no longer consistent with the thermophysical model). Lastly we notice that temperature evolutions in the gaseous medium in contact with the insulated wall are similar to the ones observed for a Dirichlet boundary condition as reported in section 4.1.2: the temperature oscillates during the first stage due to the work of compression/expansion. These compressible effects are however less pronounced than for a Dirichlet boundary condition. This is consistent with the evolution of the interface location previously discussed.

4.3 Dimensionless analysis

For sake of simplicity, we restrict ourselves to systems with $l_e^1 = l_e^2$ and temperature forcing at the left wall as in section 4.1. To summarize, three characteristic times have been derived from the analysis:

1. t_o, the inertial time, related to the oscillations frequency of the liquid layer. We have seen that the natural frequencies found in section 3 were a good estimate of the oscillation frequency of the non linear system. Therefore we take:

$$t_o = \frac{1}{f_i} = 2\pi\sqrt{\frac{m^l l_e^1 l_e^2}{P_e(l_e^1 + l_e^2)}}. \tag{50}$$

2. t_d related to heat diffusion in the heated gas and given by Eq. (44),

3. τ associated to thermal inertia of the liquid and given by Eq. (41).

Two dimensionless numbers can be established. We set :

$$N_{di} \equiv \frac{t_d}{t_o}, \quad C_{lg} \equiv \frac{\tau}{t_d}. \tag{51}$$

C_{lg} corresponds to the ratio of the heat capacities for the liquid and gas layers:

$$C_{lg} \equiv \frac{\tau}{t_d} = \frac{m^l c^l}{m^1 c_p^g}. \tag{52}$$

This number which is proportional to the density ratio ρ^l/ρ_e^1, is much greater than one. It now becomes possible to consider time evolution of the liquid layer using dimensionless quantities. The previous simulations revealed a two stage dynamics. The time scale corresponding to the end of the first stage and to the beginning of the second one has been identified to t_d. The present process involving time scales with different orders of magnitude, a logarithmic scaling appears relevant for the definition of the dimensionless time, t^*:

$$t^* = \ln(t/t_d). \tag{53}$$

With this scaling, the end of the first stage corresponds to $t^* = 0$.
We normalize the displacement using the theoretical estimate for the maximum displacement given by Eq. (43):

$$l_1^* = \frac{l^1 - l_e^1}{l_m}. \tag{54}$$

Numerical simulations with imposed temperature on the left wall are performed to investigate the influence of the numbers N_{di} and C_{lg} on the dynamics, and to verify the relevance of the proposed normalization. The reference case corresponds to the nominal situation defined in section 4.1. We then consider different values of the thermal conductivity k^g and of the specific heat capacity c^l in order to modify both N_{di} and C_{lg}. The simulation cases, labeled A to G, are summarized in Table 1.

We first examine cases A-D. Results of the numerical simulations are presented in Fig. 13 using physical variables (l^1, t) then in Fig. 14 using dimensionless variables (l_1^*, t^*). As the C_{lg} number is the same for all curves A-D, a close superimposition is observed during the second phase (Fig. 14). On the other hand, the increase of the N_{di} number from one case to another leads to significant differences between curves A-D during the first phase. This diversity deserves the following comments:

Case	N_{di}	C_{lg}	c^l (S.I.)	k^g (S.I.)	t_d (s)	τ (s)
A	1	100	542.5	$2.6\ 10^{-1}$	$9.4\ 10^{-6}$	$9.4\ 10^{-4}$
B	10	100	542.5	$2.6\ 10^{-2}$	$9.4\ 10^{-5}$	$9.4\ 10^{-3}$
C	100	100	542.5	$2.6\ 10^{-3}$	$9.4\ 10^{-4}$	$9.4\ 10^{-2}$
D	1000	100	542.5	$2.6\ 10^{-4}$	$9.4\ 10^{-3}$	$9.4\ 10^{-1}$
E	10	10	54.25	$2.6\ 10^{2}$	$9.4\ 10^{-5}$	$9.4\ 10^{-4}$
F	10	50	271.3	$2.6\ 10^{-2}$	$9.4\ 10^{-5}$	$4.68\ 10^{-3}$
G	10	1000	5425	$2.6\ 10^{-2}$	$9.4\ 10^{-5}$	$9.4\ 10^{-2}$

Table 1: Details for the numerical simulations presented in Figs. 13-15. All cases correspond to $t_o = 9.4\ \mu s$

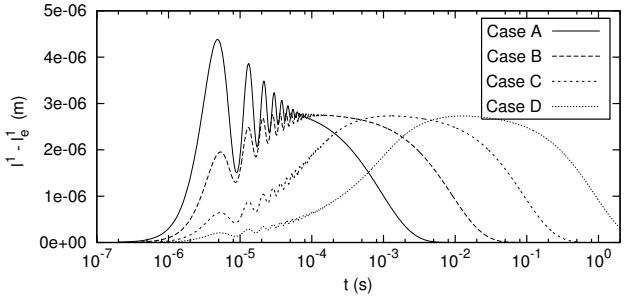

Figure 13: Evolution in time of the first interface location for Cases A-D.

- The duration of the first phase extends as the N_{di} number increases (see Fig. 13). This observation confirms the straightforward relation between the duration of the first phase and the diffusion time in the heated gas.

- For cases B, C, D, (case A will be commented later), the maximum displacement of the liquid layer coincides with the $_m$ quantity, defined in Eq. (43). This maximum is achieved at $t^* \sim 0$, *i.e.* for a physical time close to t_d. Both features are clearly evidenced by Fig. 14.

- Results presented in Fig. 13 confirm that the oscillations frequency is the same for all cases A-D. In particular the first maximum closely matches with half of the inertial time $t_o \simeq 9.4\ 10^{-6}$ s.

- The last point to be mentioned concerns the amplitude of the oscillations. Cases B, C and D

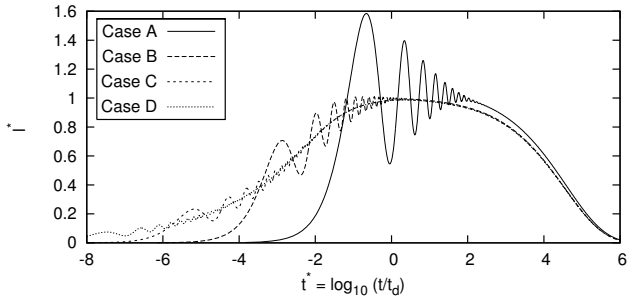

Figure 14: Evolution with the rescaled time t^* of the normalized liquid layer displacement l^* for Cases A-D.

correspond to N_{di} numbers larger than unity. This means that diffusion time t_d is higher than inertial time t_o. As a result, the liquid inclusion starts moving while heat diffusion effects are not yet perceptible in the whole gas domain (in particular, the temperature profile is not yet linear). The pressure difference between both gaseous domains decreases as the N_{di} number increases, leading to oscillations with smaller amplitude and a delayed displacement of the liquid layer (Fig. 13). Specific attention is now paid to the large oscillations displayed by curve A. Case A corresponds to a N_{di} number equal one. Thus, time for heat diffusion and time associated to the start-up motion of the liquid layer are equal: the liquid layer starts to move while temperature has already increased in the whole gaseous domain with a significant pressure rise as a result. Then, the pressure difference between the two gas layers is large leading to large accelerations of the liquid layer and intense oscillations. Note the overshoot of the $_m$ quantity, as high as 60% reached during the first oscillation.

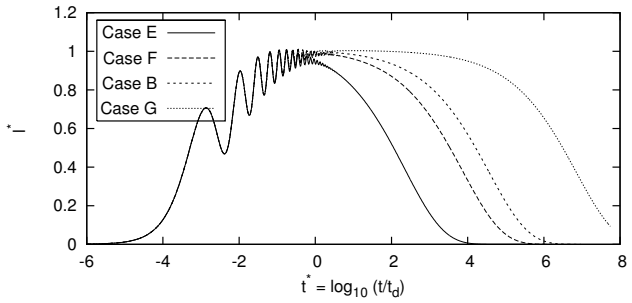

Figure 15: Evolution with the rescaled time t^* of the normalized liquid layer displacement for cases E,F,B,G.

Numerical results obtained for cases (E,F,B,G) are presented in Fig. 15 using dimensionless variables (l_1^*, t^*). These cases correspond to the same time t_o and to the same diffusion time $t_d = 10\, t_o$. This explains the perfect superimposition of the curves during the first phase. On the contrary, the relaxation time leading the system back to an equilibrium situation increases with C_{lg}. This logically stems from the definition of C_{lg} which is proportional to the characteristic time associated with thermal inertia of the liquid layer (τ). As expected from the normalization, the displacement of the liquid layer is maximum for a time close to t_d and corresponds to $_m$ defined in Eq. (43).

4.4 Step-fluxes forcing

Based on the above analysis we propose a microfluidic device performing a periodic motion of a liquid inclusion. This device uses a periodic flux forcing at the two ends of the channel. Flux forcings are considered as they are more amenable to physical experimentation than a dynamical temperature control.
The liquid layer has been shown to reach its maximum displacement $(l_m - {l^1}_e)$ for $t \sim t_d$; this suggests that heating steps with duration $\tau_p \gtrsim t_d$ should be suitable to achieve a back and forth motion of the liquid layer. Following this idea, we examine two periodic flux forcings for the nominal case ($L = 100$ μm, $l^l = 10$ μm, $l_e^1 = 45$ μm, $\rho^l = 1000$ kg m^{-3}):

- Case 1: starting from the equilibrium state, a flux $q'' = q_s$ (resp. $q'' = -q_s$) is applied at $x = 0$ (resp. $x = L$) with a duration τ_p; the fluxes are then switched off for a second time span also equal to τ_p. This cycle is repeated (see Fig. 16).

- Case 2: starting for the equilibrium state, a flux with intensity $q'' = q_s$ (resp. $q'' = 0$) is applied at $x = 0$ (resp. $x = L$) with a duration τ_p; the fluxes are then exchanged (*i.e.* $q'' = 0$ at $x = 0$ and $q'' = q_s$ at $x = L$) for another time span τ_p, before repeating the cycle (see Fig. 17).

The forcing period is thus $2\tau_p$. We set $\tau_p \sim 5t_d = 500$ μs and $q_s = 4.5\ 10^4\ Wm^{-2}$. A negative flux (*i.e.* heat extraction) can be performed in practice by the means of Peltier devices.

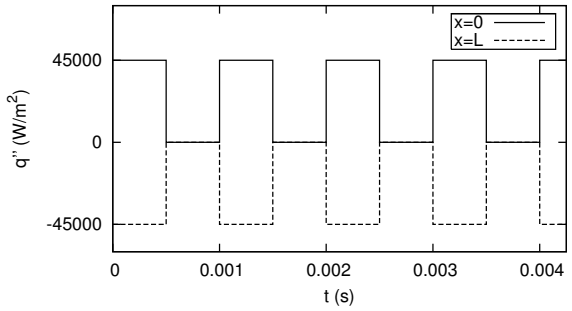

Figure 16: Heat fluxes imposed at the boundaries $x = 0$ and $x = L$ in Case 1.

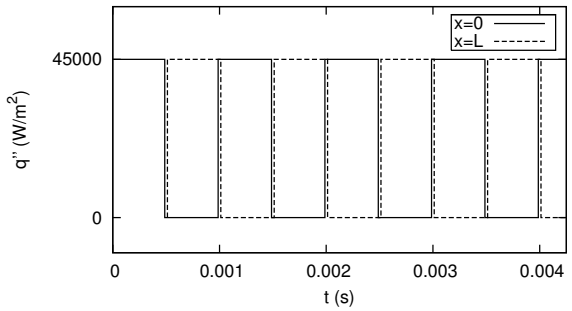

Figure 17: Heat fluxes imposed at the boundaries $x = 0$ and $x = L$ in Case 2 (signals have been slightly shifted in time for clarity).

The displacement of the first interface, as predicted by the low-Mach model for Case 1, is reported in Fig. 18. The amplitude of the displacement is roughly twice as large than for the case presented in section 4.2: the liquid layer displacement results of both the heating in Ω^1 (leading to a volume increase) *and* the cooling in Ω^2 (leading to a volume reduction). An excellent repeatability of the interface motion is achieved with these heating conditions, as the heat supplied at one end of the channel is entirely extracted at the other end. Motions of the liquid layer with constant amplitude are then achieved since the net amount of heat supplied to the system during one cycle is zero. Otherwise, the fluids get warmer (resp. cooler) as the net amount of heat supplied to the system is positive (resp. negative) and a reduction (resp. increase) of the motion amplitude results. This situation corresponds to case 2, where the net amount of heat per cycle supplied to the system is $2q_s\tau_p$. The displacements reported in Fig. 19 indeed exhibit a gradual decay as the system gets warmer. This decay is however very weak.

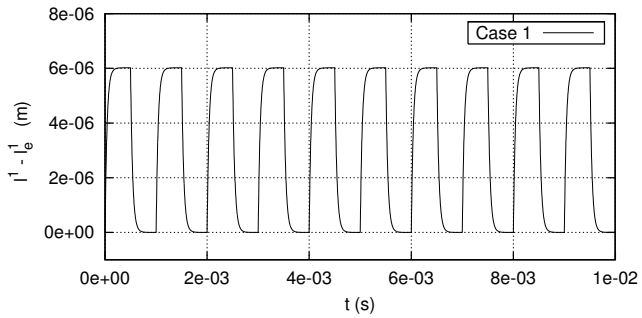

Figure 18: Displacement with time of the first interface for the forcing in Case 1.

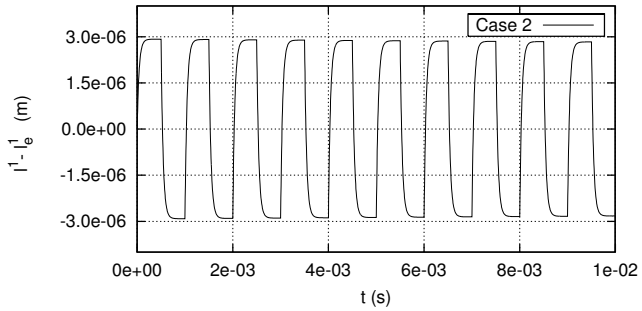

Figure 19: Displacement with time of the first interface for the forcing in Case 2. Note the damping in the displacement amplitude.

5 Conclusion

In this paper, the motion of a 1D liquid inclusion inside a closed microchannel, filled with gas, is investigated by means of theoretical analysis and numerical simulations. The simulations are based on a low-Mach approximation of the flows inside the gas domains, while the liquid domain is considered incompressible. Description of the interfaces is performed through an accurate ALE method.

The whole liquid-gas system is shown to behave as a damped oscillator. Free oscillations (*i.e.* for thermally insulated channel ends) are first investigated in the linear regime, considering uniform temperatures in the gas domains. The associated eigenmodes are identified along with the natural frequencies. The non-linear dynamics of the full system is next investigated through simulations for different heating conditions (temperature or heat-flux) at the channel ends. The main thermo-mechanical effects involved in the dynamics are identified. A scaling analysis is developed highlighting two relevant dimensionless numbers governing the dynamics. Finally, we propose suitable heating conditions to achieve oscillations of the liquid inclusion without decay. Ongoing works focus on the extension of the simulation tool for two-dimensional configurations. This requires the introduction of the wall friction and surface tension effects, as well as a different treatment of the interface dynamics.

References

[1] Canuto, C., Hussaini, M., Quarteroni, A., Zang, T.: Spectral methods in Fluids Dynamics. Springer Series in Computational Physics. Springer (1990)

[2] Chenoweth, D., Paolucci, S.: Natural convection in an enclosed vertical air layer with large horizontal temperature differences. J. Fluid Mech. **169**, 173–210 (1986)

[3] Colin, S.: Rarefaction and compressibility effects on steady and transient gas flows in microchannels. Microfluidics and Nanofluidics **1**, 268–279 (2005)

[4] Cooney, C., Towe, B.: A thermopneumatic dispensing pump. Sensors and Actuators A **116**, 519–524 (2004)

[5] Cristini, V., Tan, Y.: Theory and numerical simulation of droplets dynamics in complex flows–a review. Lab on a Chip **4**, 257–264 (2004)

[6] Daru, V., Duluc, M.C., Le Maître, O., Juric, D., Le Quéré, P.: Modélisation et simulation numérique du changement de phase liquide-vapeur en cavité. CRAS Mécanique **224**, 25–33 (2006)

[7] Erickson, D.: Towards numerical prototyping of labs-on-chip: modeling for integrated microfluidic devices. Microfluidics and Nanofluidics **1**, 301–318 (2005)

[8] Jiao, Z., Nguyen, N.T., Huang, X., Ang, Y.: Reciprocating thermocapillary plug motion in an externally heated capillary. Microfluidics and Nanofluidics **3**, 39–46 (2007)

[9] Li, Z., Ito, K.: The immersed interface method. Frontiers in Applied Mathematics. SIAM (2006)

[10] Liu, M., Liu, G.: Meshfree particle simulation of micro channel flows with surface tension. Comput. Mech. **35**, 332–341 (2005)

[11] Liu, M., Meakin, P., Huang, H.: Dissipative particle dynamics simulation of multiphase fluid flow in microchannels and microchannel network. Physics of Fluids **19** (2007)

[12] Majda, A., Sethian, J.: The derivation and numerical solution of the equations for zero Mach number combustion. Combust. Sci. Technol. **42**, 185–205 (1985)

[13] Medale, M., Jaeger, M.: Numerical simulations of incompressible flows with moving interfaces. Int. J. Num. Meth. Fluids **24**, 615–638 (1997)

[14] Mukherjee, A., Kandlikar, S.: Numerical simulation of growth of a vapor bubble during flow boiling of water in a microchannel. Microfluidics and Nanofluidics **1**, 137–145 (2005)

[15] Navti, S., Ravindran, K., Taylor, C., Lewis, R.: Finite element modelling of surface tension effects using a Lagrangian-Eulerian kinematic description. Comput. Methods Appl. Mech. Engrg. **147**, 41–60 (1997)

[16] Osher, S., Fedkiw, R.: Level set methods and dynamic implicit surface. No. 153 in Applied Mathematical Sciences. Springer (2003)

[17] Pozrikidis, C.: Boundary Integral and Singularity Methods for Linearized Viscous Flow. Cambridge University Press (1992)

[18] Scardovelli, R., Zaleski, S.: Direct numerical simulation of free-surface and interfacial flow. Ann. Rev. Fluid Mech. (31), 567–603 (1999)

[19] Selva, B., Français, O., Rousseau, L., Poulichet, P., Desportes, S., Delaire, J., Grenier, D., Jullien, M.C.: Thermal actuation in a cross-channel micromixer. In: MicroTAS (2007)

[20] Tryggvason, G., Bunner, B., Esmaeeli, A., Juric, D., Al-Rawahi, N., Tauber, W., Han, J., Nas, S., Jan, Y.: A front-tracking method for the computations of multiphase flow. J. Comput. Physics **169**(2), 708–759 (2001)

[21] Worlibar, A., Knio, O.: Numerical simulation of a thermoacoustic refrigerator: I unsteady adiabatic flow around the stack. J. Comput. Phys. **127**, 424–451 (1996)

[22] Yang, Z., Palm, B., Sehgal, B.: Numerical simulation of bubbly two-phase flow in a narrow channel. International Journal of Heat and Mass Transfer **45**, 631–639 (2002)

[23] Zheng, H., Shu, C., Chew, Y.: A lattice boltzmann model for multiphase flows with large density ratio. Journal of Computational Physics **218**, 353–371 (2006)

A Numerical Methods

The domains Ω^i moving with time, an Arbitrary Lagrangian Eulerian (ALE) method (see e.g. [15, 13]) is used for the resolution of the governing equations of the flow. Specifically, linear transformations are used to map $\Omega^1 \cup \Omega^l \cup \Omega^2$ to a reference mathematical domain $[0,1] \cup [1,2] \cup [2,3]$. The spatial discretization uses a high order spectral element for each sub-domain, with order p for the temperature, density, velocity and order $p-2$ for the hydrodynamic pressure [1]. The mapping being time dependent, it yields additional correction terms in the governing equations to account for the mesh velocity. The time integration of the flow involves diverse time discretizations and numerical methods for the inversion of the resulting discrete operators. The complete numerical methodology is detailed elsewhere, and we simply provide here a quick overview of the structure of a time step. For simplicity, we temporarily drop the domain indexes that instead will denote the time level. We assumed the solution known at time level $n\Delta t$, where Δt is the time-step of the simulation. The whole procedure for the determination of the solution at $t = (n+1)\Delta t$ is:

1. Set guessed estimates P^{n+1} for the thermodynamic pressure at the end of the time step.

2. Using P^{n+1}, update velocities and positions of the interface using a semi-implicit Newmark time-scheme. It yields the ALE mapping (geometry and mesh velocities).

3. **Prediction step:**

   - The energy equations in the sub-domains are solved for a provisional temperature field T^*, using an implicit time-scheme and Schwartz methods for the enforcement of continuity conditions across the interfaces. Other variables are taken to their respective values at $t = n\Delta t$.
   - Provisional thermodynamical pressures P^* and density fields ρ^* in the two gas domains are then determined using equation (18) and the state equation respectively.
   - Momentum equations in the gaseous domains are then solved for the provisional velocities u^* and hydrodynamic pressures Π^*. The latter is determined, through the resolution of an elliptic problem, as to yield $\frac{\partial}{\partial x}(\rho u)^*$ consistent with an estimate of $\frac{\partial}{\partial t}\rho$ based on ρ^n and ρ^*.

4. **Correction step:**

- Solve the energy equation for T^{n+1} as in the prediction step, but using the provisional values for the other variables.
- Set thermodynamical pressures P^{n+1} and density fields ρ^{n+1} in the two gas domains.
- Set the velocities u^{n+1} and hydrodynamic pressures Π^{n+1}. The latter now being determined to yield $\frac{\partial}{\partial x}(\rho u)^{n+1}$ consistent with an estimate of $\frac{\partial}{\partial t}\rho$ based on ρ^n and ρ^{n+1}.

5. If the computed thermodynamical pressures P^{n+1} are different from the ones used at step 1, restart from step 2 for a new iteration.

In the computation presented hereafter, 3 to 4 iterations were needed for the convergence of the thermodynamical pressure P^{n+1}.